

3

XFEM Formulation for Coupled Problems

This chapter focus on the theoretical formulations that give base to the implemented code in this thesis. As stated before, the eXtended Finite Element Method shares its base characteristics with the Finite Element Method. Consequently, the base concepts of the Finite Element Method (p. ex. the definition of topology or shape function) are not explained in this chapter and further reading about this may be done in works by Zienkiewicz, Taylor and Zhu (2013) or Potts and Zdravković (1999).

The physical differential equations that govern the behaviour of the implemented model are presented, as well as the developments and transformations made for them to be numerically computed. The physical equations are defined to couple both the hydro-mechanical behaviour in the porous region and in the fracture. Then the space is discretized by enrichments functions, which were established by Moes and Dolbow (1999) and Belytschko and Black (1999) and extended for intersections by Daux, Moes and Dolbow (2000), and time discretized by the Newmark technique. The set of resulting non-linear equations is linearized and solved using the Newton-Raphson method. The formulation follows the mathematical notation presented by Khoei *et al.* (2014).

Finally, the constitutive model used to simulate the behaviour of the natural fractures is presented. Although used together, the formulation for the contact and friction models is presented separately. The former is based on the penalty method while the latter uses Rueda *et al.* (2014) as reference.

3.1.

Governing equations

Modelling of hydraulic fracture propagation in porous fractured media involves coupling of various physical phenomena. In the implementation presented in this work the following effects are considered: deformation of the continuous medium, deformation and friction in the fracture, pore fluid flow through the porous

medium surrounding the fracture, fluid flow within the fracture, fluid exchange between the fracture and the surrounding porous medium, and propagation of the fracture. Two different partial differential equations are used to correctly simulate those phenomena, equilibrium equation for the mechanical behaviour and continuity equation for the fluid flow.

Some simplifications or assumptions are made. It is assumed that the porous medium is saturated and both pore and fracture flow occur under laminar regime. In addition, both grains and pore fluid have a bulk modulus which is several orders of magnitude higher than the skeleton's bulk modulus, so they can be considered incompressible. Also, all inertial effects and body forces are neglected, as the in situ stress state is defined as an input. Though relevant in certain situations, these assumptions do not substantially affect the overall behaviour of the hydraulic fracture models.

The partial differential equations apply to the generalized fractured domain defined in Figure 3.1.

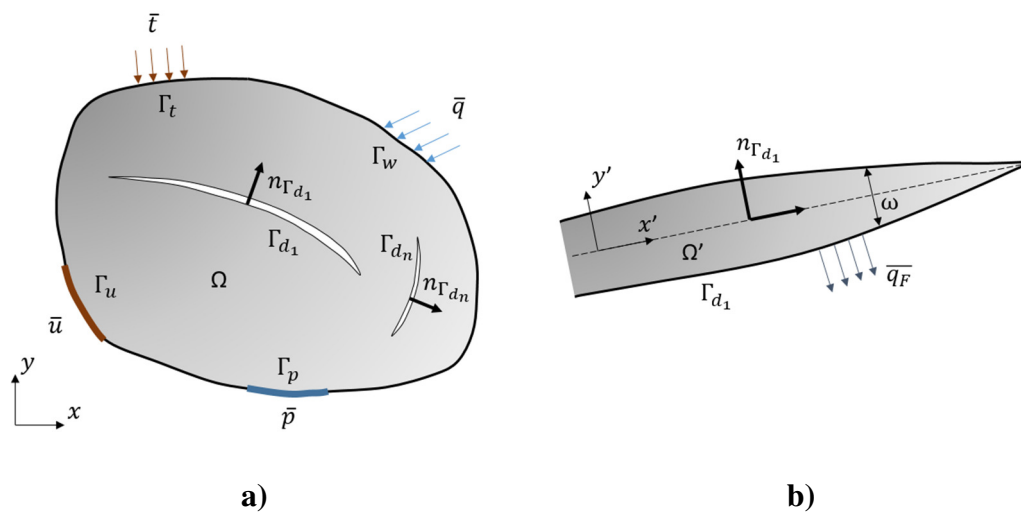


Figure 3.1 – Generalized fractured domain. a) Boundary conditions of a fractured body Ω with a geomechanical discontinuity Γ_c . b) Geometry of the fracture domain Ω' (adapted from Khoei et al. (2014))

Considering \mathbf{n}_Γ the outward unit normal vector to the general domain Ω , the boundary conditions (BC) of the domain are as follows:

- $\mathbf{u} = \bar{\mathbf{u}}$ on Γ_u (essential BC) and $\boldsymbol{\sigma} \cdot \mathbf{n}_\Gamma = \bar{\mathbf{t}}$ on Γ_t (natural BC), for the porous medium

- $\mathbf{p} = \bar{p}$ on Γ_p (essential BC) and $\dot{\mathbf{w}} \cdot \mathbf{n}_\Gamma = \bar{q}$ on Γ_w (natural BC), for the fluid phase

Additional BC apply to the discontinuities having \mathbf{n}_{Γ_d} as the unit normal vector which points to the positive side Ω^+ and $[[\dot{\mathbf{w}}]]$ as the jump of fluid velocity in the discontinuity:

- $\boldsymbol{\sigma} \cdot \mathbf{n}_{\Gamma_d} = -\mathbf{p}_F \cdot \mathbf{n}_{\Gamma_d}$ and $[[\dot{\mathbf{w}}]] \cdot \mathbf{n}_{\Gamma_d} = \bar{q}_F$ on Γ_d (natural BC).

The linear momentum balance that characterizes the mechanical behaviour of the porous medium is given by

$$\nabla \cdot \boldsymbol{\sigma} = 0 \quad (3.1)$$

where $\boldsymbol{\sigma}$ is the stress tensor and ∇ the vector gradient operator.

The total stress tensor may be defined as $\boldsymbol{\sigma} = \boldsymbol{\sigma}' - p \cdot \mathbf{I}$, where $\boldsymbol{\sigma}'$ is the effective stress tensor, p the average pressure of pore fluid and \mathbf{I} the identity matrix. In this context, compressive stresses are negative.

The continuity equation governs the fluid phase. Although belonging to the same phase, different equations describe porous and fracture flow. This allows representing loss of pressure between fracture faces and surrounding porous medium, as the filter cake effect. Considering a saturated medium with incompressible fluid, the simplified continuity equation for the porous and the fracture flow follows

$$\nabla \cdot \dot{\mathbf{w}} + \nabla \cdot \dot{\mathbf{u}} = 0 \quad (3.2)$$

where $\dot{\mathbf{w}}$ is the fluid velocity, while $\dot{\mathbf{u}}$ is the solid-fluid mixture velocity, if the equation is applied on the porous or the fracture domain, or the fracture opening velocity, if on the fracture domain.

The constitutive mechanical equation for the porous medium is introduced as the strain- effective stress relationship in Eq. (3.3), where \mathbf{D} is a fourth order tangential stiffness matrix of the bulk material. Due to assumption of small strains and displacements the strain-displacement kinematic relation is given by Eq. (3.4), where ∇_s is the symmetric part of the gradient operator. The mechanical behaviour of the fracture is given by a traction-displacement relationship, such as the one in Eq. (3.5) where \mathbf{D}_F represents a second order tangential stiffness matrix, \mathbf{t}_F the fracture tractions and $[[u]]$ the fracture relative displacements.

$$d\boldsymbol{\sigma}' = \mathbf{D} \cdot d\boldsymbol{\varepsilon} \quad (3.3)$$

$$\boldsymbol{\varepsilon} = \nabla_s \mathbf{u} \quad (3.4)$$

$$d\mathbf{t}_F = \mathbf{D}_F \cdot d[\mathbf{u}] \quad (3.5)$$

$$\dot{\mathbf{w}} = -\mathbf{k} \cdot \nabla \mathbf{p} \quad (3.6)$$

One further assumption is laminar flow without gravitational effects both in the porous medium and in the fracture medium, following Darcy's Law, Eq. (3.6), where \mathbf{p} is the pressure and \mathbf{q} the flow rate. The variable \mathbf{k} depends on the domain of interest:

- In the porous medium, it represents the hydraulic conductivity matrix (\mathbf{k}_f), which is given by the constant second order matrix

$$\begin{bmatrix} k_x & 0 \\ 0 & k_y \end{bmatrix}$$

- In the fracture tangential direction, \mathbf{k} represents the fracture longitudinal transmissibility, which affects the longitudinal flow represented in Figure 3.2a. This is a scalar that is assumed to follow a cubic law, depending on the fracture aperture ω and fluid dynamic viscosity μ , given by Eq. (3.7).

$$k_{fF} = \omega^2 / 12\mu \quad (3.7)$$

- In the fracture-porous region interface, it represents the conductivity of a very thin layer that causes loss of pressure in the flow transversal to the fracture (see Figure 3.2b). A scalar parameter c , named fracture face transversal conductivity, quantifies this effect. Although having different dimensions, this parameter is physically similar to the so-called leak-off coefficient. Considering p_F the fluid pressure in the discontinuity, p the pressure in the surrounding porous region and q_F as the flow rate between both, the adaptation of Darcy's equation gives

$$q_F = c(p - p_F) \quad (3.8)$$

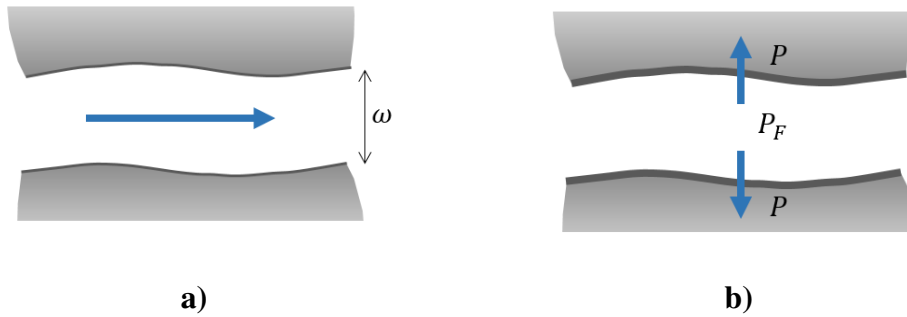


Figure 3.2 – Representation of fracture flow. a) Longitudinal flow. b) Transversal flow

3.2. Weak formulation

The weak form of the governing differential equations is obtained by integrating the product between each equation and admissible test functions. Then, in order to represent correctly the fractured domain, the Divergence Theorem for discontinuous functions is applied, as given in Eq. (3.9), in order to correctly represent the fractured domain.

$$\int_{\Omega} \operatorname{div} \mathbf{F} \, d\Omega = \int_{\Gamma} \mathbf{F} \cdot \mathbf{n}_{\Gamma} \, d\Gamma - \int_{\Gamma_d} \llbracket \mathbf{F} \rrbracket \cdot \mathbf{n}_{\Gamma_d} \, d\Gamma \quad (3.9)$$

$$\int_{\Omega} \operatorname{div} \mathbf{F} \, d\Omega = \int_{\Gamma} \mathbf{F} \cdot \mathbf{n}_{\Gamma} \, d\Gamma - \sum_i^{N_c} \int_{\Gamma_{d_i}} \llbracket \mathbf{F}_i \rrbracket \cdot \mathbf{n}_{\Gamma_{d_i}} \, d\Gamma \quad (3.10)$$

$\llbracket \mathbf{F} \rrbracket$ represents the jump of the function \mathbf{F} , being $\llbracket \mathbf{F} \rrbracket = \mathbf{F}^+ - \mathbf{F}^-$, i.e. \mathbf{F}^+ is the value of \mathbf{F} at the boundary \mathbf{n}_{Γ}^+ and \mathbf{F}^- is the value of \mathbf{F} at \mathbf{n}_{Γ}^- . If more than one discontinuity exists, the Divergence Theorem may be generalized to Eq. (3.10), where N_c is the number of discontinuities in the domain.

Defining $\mathbf{u}(\mathbf{x}, t)$, $p(\mathbf{x}, t)$ and $p_F(x, t)$ as trial functions and $\delta \mathbf{u}(\mathbf{x}, t)$, $\delta p(\mathbf{x}, t)$ and $\delta p_F(x, t)$ as test functions and integrating over the domain Ω , the weak form of equations (3.1) and (3.2) is respectively

$$\int_{\Omega} \delta \mathbf{u}(\nabla \cdot \boldsymbol{\sigma}) \, d\Omega = 0 \quad (3.11)$$

$$\int_{\Omega} \delta p(\nabla \cdot \dot{\mathbf{w}} + \nabla \cdot \dot{\mathbf{u}}) \, d\Omega = 0 \quad (3.12)$$

As for the fracture domain Ω' presented in Figure 3.1b, the weak form of equation (3.2) is

$$\int_{\Omega'} \delta p_F (\nabla \cdot \dot{\mathbf{w}} + \nabla \cdot \dot{\mathbf{u}}) d\Omega = 0 \quad (3.13)$$

Applying to Eqs. (3.11) to (3.13) the mechanical and hydraulic constitutive relationships, Eqs. (3.3) to (3.8), in the continuous region and in the fracture, gives

$$\begin{aligned} \int_{\Omega} \delta \boldsymbol{\varepsilon} \cdot \boldsymbol{\sigma}' d\Omega - \int_{\Omega} \delta \boldsymbol{\varepsilon} \cdot m \cdot p d\Omega + \int_{\Gamma_d} \llbracket \delta \mathbf{u} \rrbracket (\mathbf{t}_F - p_F \cdot \mathbf{n}_{\Gamma_d}) d\Gamma \\ - \int_{\Gamma_t} \delta \mathbf{u} \cdot \bar{\mathbf{t}} d\Gamma = 0 \end{aligned} \quad (3.14)$$

$$\begin{aligned} \int_{\Omega} \nabla \delta p k_f \nabla p d\Omega + \int_{\Gamma_d} \delta p \llbracket \dot{\mathbf{w}} \rrbracket \mathbf{n}_{\Gamma_d} d\Gamma + \int_{\Omega} \delta p \cdot \nabla \dot{\mathbf{u}} d\Omega \\ + \int_{\Gamma_w} \delta p \cdot \bar{q} d\Gamma = 0 \end{aligned} \quad (3.15)$$

$$\int_{\Omega'} \nabla \delta p_F k_{f_F} \nabla p_F d\Omega - \int_{\Gamma_d} \delta p_F \llbracket \dot{\mathbf{w}} \rrbracket \mathbf{n}_{\Gamma_d} d\Gamma + \int_{\Omega'} \delta p_F \nabla \dot{\mathbf{u}} d\Omega = 0 \quad (3.16)$$

For simplicity, Eqs. (3.14) to (3.16) reflect the presence of one discontinuity. However, this formulation may be generalized to any number of discontinuities, according to Eq. (3.10). At this point, the hydro-mechanical coupling is evident in each equation. In Eq. (3.14) the hydraulic coupling arises from the pore and fracture pressures, which are present in the second and third term, respectively. In Eq. (3.15) the fluid exchange through the fracture wall is in the second term, followed by the mechanical coupling in the third term. Finally, in Eq. (3.16) the fluid exchange with the porous medium is in the second term – repeating the exchange term of Eq. (3.15) – and the fracture deformation in the third term.

Considering the integrals over the discontinuity domain (Ω') presented in Eq. (3.16) and the fact that discontinuities have an aperture many orders of magnitude smaller than the other dimensions, a simplification is convenient. It consists in assuming the fluid pressures along the discontinuity cross section as constant, reducing the integration domain in one order – from Ω' to Γ . Thus, the first and third term of Eq. (3.16) are redefined as

$$\int_{\Omega'} \nabla \delta p_F k_{fF} \nabla p_F d\Omega = \int_{\Gamma_d} \frac{\partial \delta p_F}{\partial x'} k_{fF} \cdot 2h \cdot \frac{\partial p_F}{\partial x'} d\Gamma \quad (3.17)$$

$$\int_{\Omega'} \delta p_F \cdot \nabla \dot{\mathbf{u}} d\Omega = \int_{\Gamma_d} \delta p_F \cdot 2h \cdot \left\langle \frac{\partial \dot{u}_{x'}}{\partial x'} \right\rangle d\Gamma + \int_{\Gamma_d} \delta p_F \cdot \llbracket \dot{u}_{y'} \rrbracket d\Gamma \quad (3.18)$$

where x' and y' are the local coordinates of the discontinuity, as seen in Figure 3.1b, and h is the half-aperture of the fracture. The local x' and y' components of the velocity vector projected on the longitudinal and transversal directions are $\dot{u}_{x'}$ and $\dot{u}_{y'}$, respectively, which are assumed to vary linearly in the transversal direction. According to this hypothesis, the derivative of the velocity in x' direction may take an average value $\langle \mathcal{E} \rangle = (\mathcal{E}^+ + \mathcal{E}^-)/2$. Substituting the redefined terms in Eq. (3.16) and taking the flow rate jump, i.e. the flow through the fracture faces, as $\llbracket \dot{\mathbf{w}} \rrbracket = q_F$, gives the following equation

$$\begin{aligned} \int_{\Gamma_d} \frac{\partial \delta p_F}{\partial x'} k_{fF} \cdot 2h \cdot \frac{\partial p_F}{\partial x'} d\Gamma - \int_{\Gamma_d} \delta p_F q_F \mathbf{n}_{\Gamma d} d\Gamma \\ + \int_{\Gamma_d} \delta p_F \cdot 2h \cdot \left\langle \frac{\partial \dot{u}_{x'}}{\partial x'} \right\rangle d\Gamma + \int_{\Gamma_d} \delta p_F \cdot \llbracket \dot{u}_{y'} \rrbracket d\Gamma = 0 \end{aligned} \quad (3.19)$$

3.3. Spatial discretization

3.3.1. XFEM discretization

The eXtended Finite Element Method (XFEM) to discretize Eqs (3.14), (3.15) and (3.19) consists in adopting special spatial discretization fields. In the standard FEM, the displacement and pressure fields, $\mathbf{u}(\mathbf{x}, t)$ and $\mathbf{p}(\mathbf{x}, t)$, respectively, within an element are given by the product between the vector of node variables in one element $u_i(t)$ and shape functions related to each node N_i , as Eq. (3.20) shows. \mathcal{N} is the set of all nodal points in the domain.

$$\mathbf{u}(\mathbf{x}, t) = \sum_{i \in \mathcal{N}} u_i(t) \cdot N_i \quad (3.20)$$

Independently of the number of nodes per element, the shape functions used in the standard FEM are smooth and continuous. As a consequence, the resulting fields are also continuous. Figure 3.3 shows an example of the values along the

element of a shape function for a node i , considering a 4-node element. Three perspectives are presented for easiness of understanding.

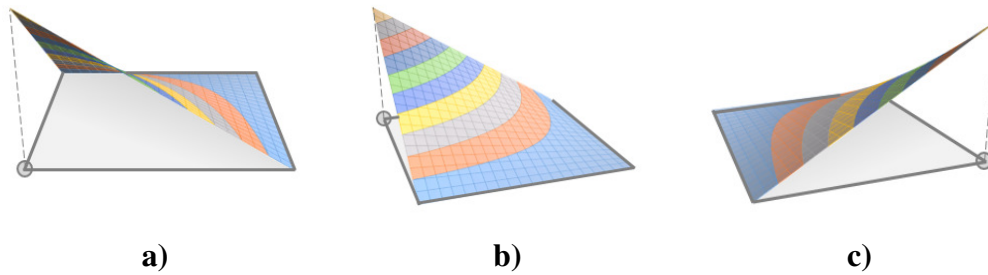


Figure 3.3 – Value of shape function in node i for a 4-node element. a) View 0°. b) View 70°. c) View 250°

The basic idea of the XFEM is to change shape functions to represent discontinuities in the displacement fields (or any other variable). For example, in order to represent a fracture explicitly within one element, for each standard degree of freedom the XFEM considers an additional degree of freedom (or “enriched degree of freedom”) which is multiplied by a discontinuous shape function, as seen in Eq. (3.21).

$$\mathbf{u}(\mathbf{x}, t) = \sum_{i \in \mathcal{N}} u_i(t) \cdot N_{u_i}^{std} + \sum_{j \in \mathcal{N}^{dis}} a_j(t) \cdot N_{u_j}^{enr} \quad (3.21)$$

This provides a discontinuous field that represents the jump in the displacement field given by the fracture faces. The additional degrees of freedom a_j are often called “enriched degrees of freedom” and the enriched shape function $N_{u_j}^{enr}$ is given by the product between the standard shape functions $N_{u_j}^{std}$ and an enrichment function ϑ , as seen in Eq. (3.22). The influence of these degrees of freedom is only considered in the \mathcal{N}^{dis} , which is the set of nodes whose support is bisected by the crack as seen in Figure 3.4.

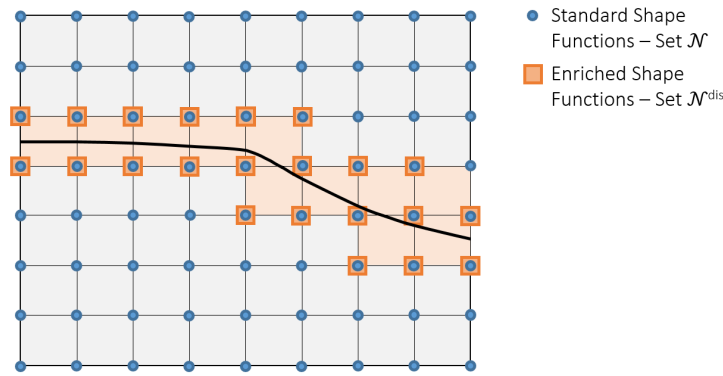


Figure 3.4 – Standard and Enriched degrees of freedom and their positions

It should be highlighted that the shape function N_u^{std} used to define the enriched shape function N_u^{enr} does not have to be the standard shape function. However, in this work, the standard shape functions are also used to compute the enriched shape functions.

$$N_u^{enr} = N_u^{std} \cdot \vartheta \quad (3.22)$$

According to Fries and Belytschko (2010), the approximation presented in Eq. (3.21) can reproduce any enrichment function exactly in Ω as long as the Partition of Unity is valid, i.e.

$$\sum_{j \in \mathcal{N}^{dis}} N_{u_j}^{enr} = 1 \quad (3.23)$$

3.3.2. Enrichment functions

As the XFEM is generalized for any kind of enrichment function ϑ , proper functions must be defined considering the type of problem of interest. In this study, only linear quadrilateral elements are used, i.e. 4 node elements, so it must be considered that the chosen enrichment functions are multiplied by linear shape functions.

For the simulation of hydraulic or natural fractures these functions must meet the following requirements: 1) show a discontinuity in the fracture position; 2) have a discontinuous derivative in the fracture position; and 3) be linear on each side of the fracture. A signed level set function guarantees these conditions.

$$\varphi(x) = \min\|x - x^*\| \cdot \text{sign}\left((x - x^*) \cdot \mathbf{n}_{\Gamma_d}\right) \quad (3.24)$$

The level set function for a point x is the closest distance to the point x^* located on the discontinuity. The signed level set function H is

$$H(\varphi(x)) = \begin{cases} +1, & \varphi(x) \geq 0 \\ -1, & \varphi(x) < 0 \end{cases} \quad (3.25)$$

As for the pore pressure fields, two different types of patterns are expected to occur in the studied problems. For the sake of simplicity, these will be called hydraulic fracture type and natural fracture type. Fluid injection in hydraulic fractures usually induces longitudinal and transversal flow. This leads to high pressures inside the fracture, which dissipate in the surrounding porous medium (Figure 3.5a). Furthermore, the possible occurrence of a filter cake may lead to loss of pressure on the fracture faces. As seen in Figure 3.5b, this loss of pressure may be different on both faces of the fracture. The hydraulic or mechanical conditions may also differ between fracture faces, resulting in $P_A \neq P_B$ (Figure 3.5c).

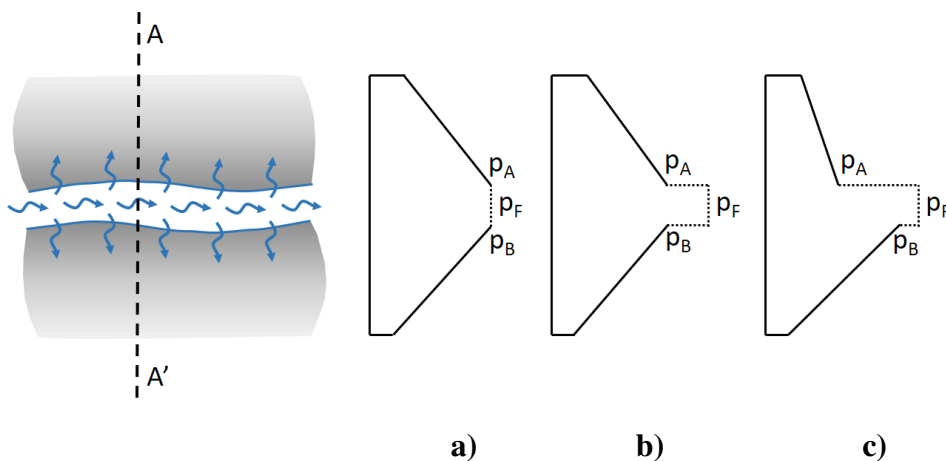


Figure 3.5 – Pore pressure patterns (section A-A') near a hydraulic fracture. a) Filter cake not considered. b) Filter cake with loss of pressure. c) Filter cake with different top and bottom leak-off conditions

In natural fractures, a different pattern is expected. In the cases of dominant transversal flow, loss of pressure related to the fracture may be significant or not, as seen in Figure 3.6. Regarding the focus of this research on studying the intersection between hydraulic and natural fractures, high pressures inside a natural fracture may occur, causing a change of behaviour from the patterns represented in Figure 3.6 to the ones presented in Figure 3.5.

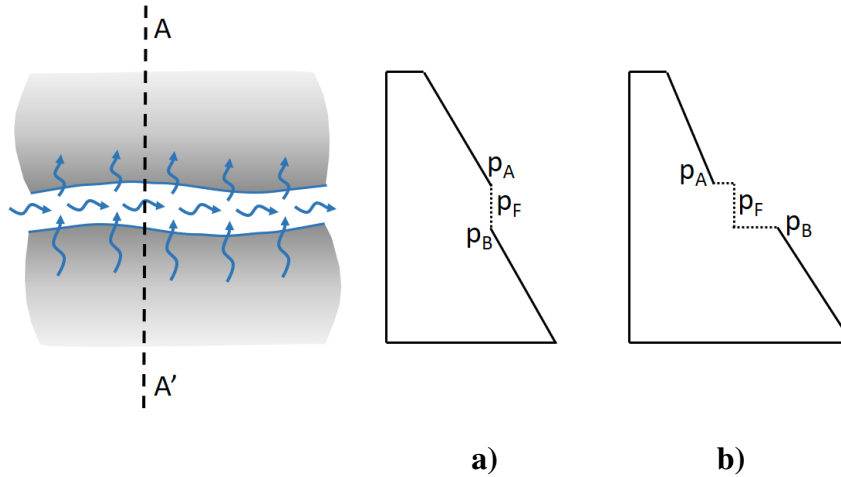


Figure 3.6 – Pore pressure patterns (section A-A’) near a natural fracture. a) Without loss of pressure through the fracture. b) With loss of pressure in the fracture

Based on these considerations, the pore pressure field of a fractured element must: 1) show a discontinuity in the fracture position; 2) have a derivative which is discontinuous at the fracture face; and 3) be linear at each side of the fracture. These are the same conditions as those for the displacement fields. Consequently, the same enrichment function (signed level set function H) is adequate to represent the pore pressure fields in a fractured domain.

For hydro-mechanical coupling in the element domain, it may be stated that the sets \mathcal{N} and \mathcal{N}^{dis} are the same for both mechanical and hydraulic discretization, (3.26) and (3.27), respectively.

$$\mathbf{u}(\mathbf{x}, t) = \sum_{i \in \mathcal{N}} u_i(t) \cdot N_{u_i}^{std} + \sum_{j \in \mathcal{N}^{dis}} a_j(t) \cdot N_{u_j}^{std} \cdot H(x) \quad (3.26)$$

$$\mathbf{p}(\mathbf{x}, t) = \sum_{i \in \mathcal{N}} p_i(t) \cdot N_{p_i}^{std} + \sum_{j \in \mathcal{N}^{dis}} p_{a_j}(t) \cdot N_{p_j}^{std} \cdot H(x) \quad (3.27)$$

As stated by Belytschko *et al.* (2001), it is beneficial to replace the enrichment function in Eqs. (3.26) and (3.27) by $(H(x) - H_j)$. The enrichment function then vanishes in all elements except those that contain the discontinuity. Another advantage is that the enrichment variable vanishes in the nodal points, which means that the interpretation of the results on those nodes only depends on the standard part of the solution. This variation, often called shifted formulation, is applied in all

enrichments used in this work. However, for the sake of notation simplicity, the shifted formulation is represented by H in further developments.

It should be highlighted that, since only a sign function is used to enrich the degrees of freedom, there should not be a concern about blending elements, i.e. the non-fractured elements that have coincident nodes with enriched elements. As stated by Fries (2008), the sign enrichment is a special case that does not lead to problems in blending elements. The reason is that the sign enrichment is a constant function in the blending elements and as long as the partition of unity functions are of the same or lower order than the shape functions, the unwanted terms in the blending elements can be compensated.

From Eq. (3.10) it is noticeable that the coupled hydro-mechanical problem may be expanded to several fractures in the domain. Eq. (3.28) presents the displacement discretization of a domain with N_c fractures.

$$\mathbf{u}(\mathbf{x}, t) = \sum_{i \in \mathcal{N}} u_i(t) \cdot N_{u_i}^{std} + \sum_{k=1}^{N_c} \sum_{j \in \mathcal{N}^{dis}} a_{j,k}(t) \cdot N_{u_j}^{std} \cdot H_k(x) \quad (3.28)$$

Figure 3.7 shows the values of the shape function for a node j multiplied by the enrichment shifted function $(H(x) - H_j)$, considering a 4-node element.

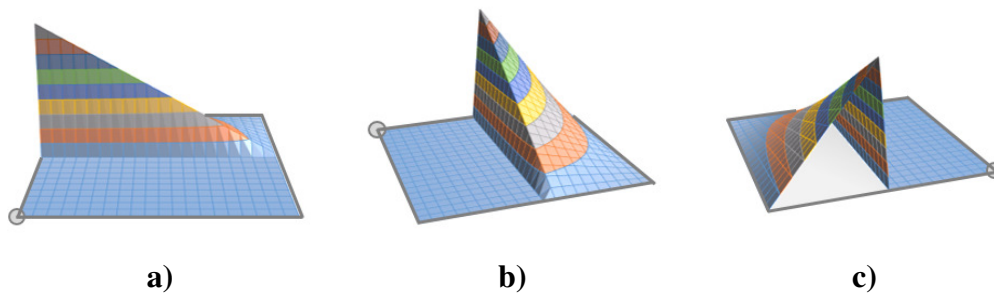


Figure 3.7 – Value of shape function in node j multiplied by the enrichment shifted function $(H(x) - H_j)$ for 4-node element. a) View 0° . b) View 70° . c) View 250°

3.3.3. Intersections

If fractures intersect each other, then the discretization needs to be adapted so it represents the intersections correctly. A junction enrichment function, J , represents an intersection between two fractures (Daux, Moes and Dolbow, 2000).

This function depends on the enrichment functions of each fracture, H_I and H_{II} , as Eq. (3.29) and Figure 3.8 present.

$$J(x) = \begin{cases} 0, & H_I(x) \geq 0 \\ H_{II}(x), & H_I(x) < 0 \end{cases} \quad (3.29)$$

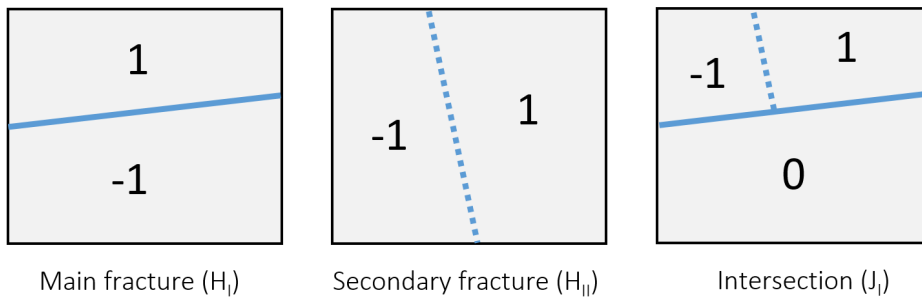


Figure 3.8 – Enrichment function J (adapted from (Daux, Moes and Dolbow, 2000))

Figure 3.9 shows the values along the element of a shape function for a node j multiplied by the enrichment shifted function $(J(x) - J_j)$, considering a 4-node element.

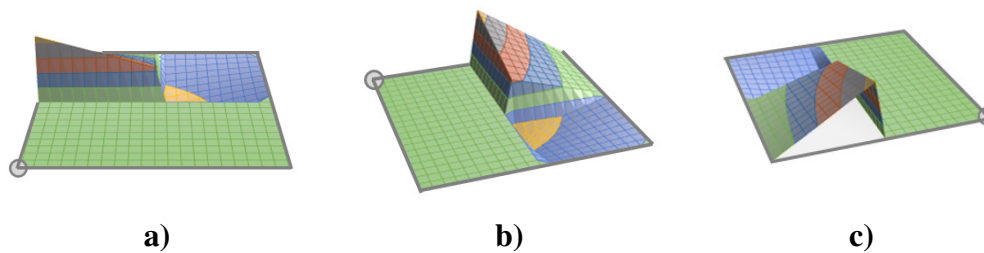


Figure 3.9 – Value of shape function in node j multiplied by the enrichment shifted function $(J(x) - J_j)$ for a 4-node element. a) View 0°. b) View 70°. c) View 250°

The application of the new enrichment function, requires a new set of degrees of freedom \mathcal{N}^{int} . Figure 3.10 pictures the different enhanced degrees of freedom and shape functions for an intersection situation.

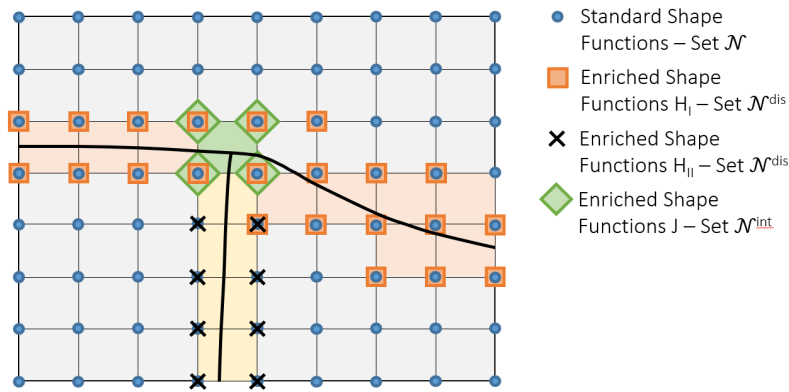


Figure 3.10 – Intersection enriched degrees of freedom and their positions

The generalization of the junction enrichment functions for a number of fracture intersections is straightforward. Yet, a particular case requires special attention. When one fracture crosses another, this must be treated as two different intersections. In this way, one main and two secondary fractures are defined. Thus, different junction enrichments J_I and J_{II} describe the intersection between the main fracture and each secondary fracture. Figure 3.11 shows this pattern and the enrichment functions.

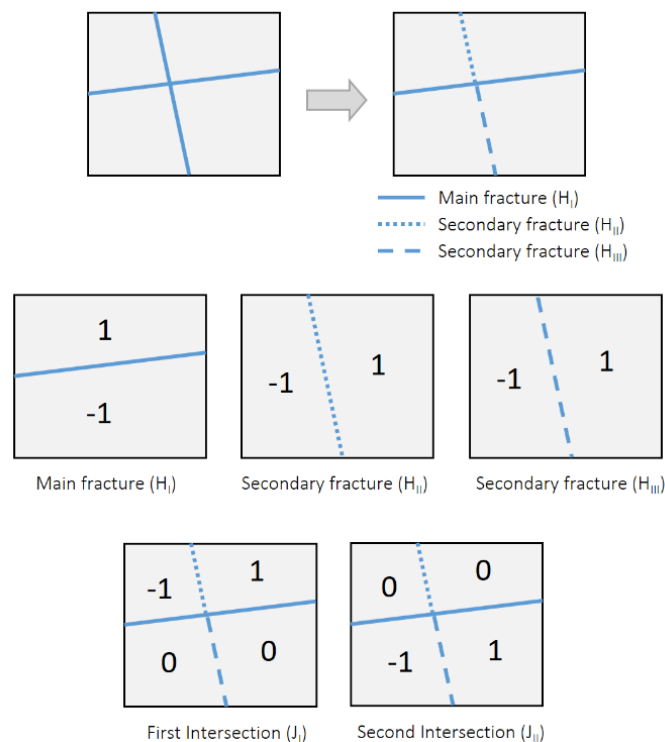


Figure 3.11 – Secondary fracture enrichment when crossing occurs

Each fracture intersection requires a new enriched degree of freedom b related to a specific enrichment function J . Eq. (3.30) provides the displacement field generalized for N_x intersections and N_c fractures.

$$\begin{aligned} \mathbf{u}(\mathbf{x}, t) = & \sum_{i \in \mathcal{N}} u_i(t) \cdot N_{u_i}^{std} + \sum_{k=1}^{N_c} \sum_{j \in \mathcal{N}^{dis}} a_{j,k}(t) \cdot N_{u_j}^{std} \cdot H_k(\mathbf{x}) \\ & + \sum_{k=1}^{N_x} \sum_{j \in \mathcal{N}^{int}} b_{j,k}(t) \cdot N_{u_j}^{std} \cdot J_k(\mathbf{x}) \end{aligned} \quad (3.30)$$

All considerations regarding enrichment functions and discretizations for displacements are considered applicable to the pore pressure discretization at intersections, once the pore pressure enrichment functions are the same. Consequently, the discretization of a pore pressure field with intersecting discontinuities follows

$$\begin{aligned} \mathbf{p}(\mathbf{x}, t) = & \sum_{i \in \mathcal{N}} p_i(t) \cdot N_{p_i}^{std} + \sum_{k=1}^{N_c} \sum_{j \in \mathcal{N}^{dis}} p_{a_{j,k}}(t) \cdot N_{p_j}^{std} \cdot H_k(\mathbf{x}) \\ & + \sum_{k=1}^{N_x} \sum_{j \in \mathcal{N}^{int}} p_{b_{j,k}}(t) \cdot N_{p_j}^{std} \cdot J_k(\mathbf{x}) \end{aligned} \quad (3.31)$$

3.3.4. Fracture discretization

Unlike the displacements and pore pressures, which are integrated in the domain Ω , the fracture fluid pressures, given by p_F , are integrated and discretized within the fracture level Γ . This allows the consideration of a jump between the fracture pressure and the surrounding pore pressures, as observed in Figure 3.5c. The discretization of the fracture pressure using Eq. (3.32), new degrees of freedom are placed at every intersection between the fracture and the element sides. Additional degrees of freedom are introduced at intersections between fractures, as Figure 3.12 presents.

$$p_F(\mathbf{x}, t) = \sum_{i \in \mathcal{N}^d} p_{F_i}(t) \cdot N_{p_{F_i}}^{std} \quad (3.32)$$

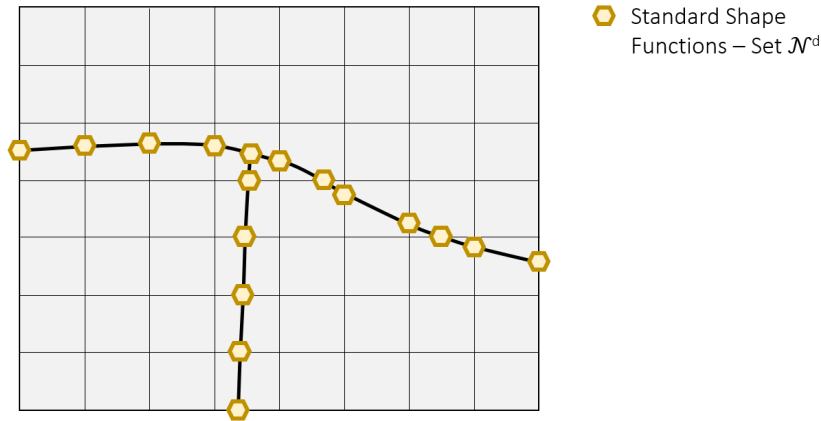


Figure 3.12 –Fracture pressure degrees of freedom and their positions

3.3.5. Resulting space discretization

Without loss of generality the test functions $\delta \mathbf{u}$, $\delta \mathbf{p}$ and δp_F follow the same discretization rules as the corresponding fields. Thus, the substitution of the discrete fields and their derivatives in Eqs. (3.14), (3.15) and (3.19) gives the following non-linear system of equations (see Annex A for details)

$$[\mathbf{K}]\{\bar{\mathbf{U}}\} - [\mathbf{Q}]\{\bar{\mathbf{P}}\} + \mathbf{f}_{\bar{\mathbf{U}}}^{\text{int}} - \mathbf{f}_{\bar{\mathbf{U}}}^{\text{ext}} = 0 \quad (3.33)$$

$$[\mathbf{Q}^T]\{\dot{\bar{\mathbf{U}}}\} + [\mathbf{H} + \mathbf{L1}]\{\bar{\mathbf{P}}\} - [\mathbf{L2}]\{\bar{\mathbf{P}}_F\} - \mathbf{q}_{\bar{\mathbf{P}}}^{\text{ext}} = 0 \quad (3.34)$$

$$-[\mathbf{L2}^T]\{\bar{\mathbf{P}}\} + [\mathbf{H}_F + \mathbf{L3}]\{\bar{\mathbf{P}}_F\} - \mathbf{q}_{\bar{\mathbf{P}}_F}^{\text{int}} = 0 \quad (3.35)$$

3.4. Time discretization

The volume-related terms in the formulation ($\dot{\mathbf{u}}$, $\dot{\mathbf{a}}$, $[[\dot{\mathbf{u}}]]$, and $\langle \nabla \dot{\mathbf{u}} \rangle$) require a time discretization. In this work a first order Generalized Newmark scheme (GN11) is employed for the displacement field, as seen in Eq. (3.36). This relation establishes a relation between two consecutive time steps n and $n+1$, whose time value is, respectively, t_{n+1} and t_n , with $\Delta t = t_{n+1} - t_n$.

$$\dot{\bar{\mathbf{U}}}_{n+1} = \frac{\gamma}{\beta \Delta t} (\bar{\mathbf{U}}_{n+1} - \bar{\mathbf{U}}_n) - \left(\frac{\gamma}{\beta} - 1 \right) \dot{\bar{\mathbf{U}}}_n \quad (3.36)$$

According to Zienkiewicz, Taylor and Zhu (2013), the solution is implicit and unconditionally stable for $\beta = \gamma = \theta = 1$, then

$$\dot{\bar{U}}_{n+1} = \frac{(\bar{U}_{n+1} - \bar{U}_n)}{\Delta t} \quad (3.37)$$

Attributing the time index and substituting Eq. (3.37) in Eq. (3.34), the following equations are obtained

$$\Psi_{\bar{U}_{n+1}} = \mathbf{K}\bar{U}_{n+1} - \mathbf{Q}\bar{\mathbb{P}}_{n+1} + \mathbf{f}_{\bar{U}_{n+1}}^{\text{int}} - \mathbf{f}_{\bar{U}_{n+1}}^{\text{ext}} = 0 \quad (3.38)$$

$$\begin{aligned} \Psi_{\bar{\mathbb{P}}_{n+1}} &= \frac{1}{\Delta t} \mathbf{Q}^T \bar{U}_{n+1} + (\mathbf{H} + \mathbf{L1})\bar{\mathbb{P}}_{n+1} - \mathbf{L2}\bar{\mathbb{P}}_{F_{n+1}} - \mathbf{q}_{\bar{\mathbb{P}}_{n+1}}^{\text{ext}} \\ &\quad - \frac{1}{\Delta t} \mathbf{Q}^T \bar{U}_n = 0 \end{aligned} \quad (3.39)$$

$$\Psi_{\bar{\mathbb{P}}_{F_{n+1}}} = -\mathbf{L2}^T \bar{\mathbb{P}}_{n+1} + (\mathbf{H}_F + \mathbf{L3})\bar{\mathbb{P}}_{F_{n+1}} - \mathbf{q}_{\bar{\mathbb{P}}_{F_{n+1}}}^{\text{int}} = 0 \quad (3.40)$$

3.5. Newton-Raphson algorithm

The set of Eqs. (3.38), (3.39) and (3.40) may be non-linear if at least one of three conditions occur: material non-linearity in the porous region – Eq. (3.3), material non-linearity in the fracture region – Eq. (3.5), or fracture longitudinal transmissibility depending on fracture aperture – Eq. (3.7). In this case, the equations need to be linearized in order to be solved. The Newton-Raphson iterative algorithm solves the system of discrete non-linear equations. By expanding Eqs. (3.38), (3.39) and (3.40) with the first-order truncated Taylor series, the linear approximation of the coupled system is obtained

$$\begin{aligned} \begin{Bmatrix} \Psi_{\bar{U}_{n+1}}^{i+1} \\ \Psi_{\bar{\mathbb{P}}_{n+1}}^{i+1} \\ \Psi_{\bar{\mathbb{P}}_{F_{n+1}}}^{i+1} \end{Bmatrix} &= \begin{Bmatrix} \Psi_{\bar{U}_{n+1}}^i \\ \Psi_{\bar{\mathbb{P}}_{n+1}}^i \\ \Psi_{\bar{\mathbb{P}}_{F_{n+1}}}^i \end{Bmatrix} + \begin{bmatrix} \frac{\partial \Psi_{\bar{U}}}{\partial \bar{U}} & \frac{\partial \Psi_{\bar{U}}}{\partial \bar{\mathbb{P}}} & \frac{\partial \Psi_{\bar{U}}}{\partial \bar{\mathbb{P}}_F} \\ \frac{\partial \Psi_{\bar{\mathbb{P}}}}{\partial \bar{U}} & \frac{\partial \Psi_{\bar{\mathbb{P}}}}{\partial \bar{\mathbb{P}}} & \frac{\partial \Psi_{\bar{\mathbb{P}}}}{\partial \bar{\mathbb{P}}_F} \\ \frac{\partial \Psi_{\bar{\mathbb{P}}_F}}{\partial \bar{U}} & \frac{\partial \Psi_{\bar{\mathbb{P}}_F}}{\partial \bar{\mathbb{P}}} & \frac{\partial \Psi_{\bar{\mathbb{P}}_F}}{\partial \bar{\mathbb{P}}_F} \end{bmatrix}_{n+1}^i \begin{Bmatrix} d\bar{U}_n^i \\ d\bar{\mathbb{P}}_n^i \\ d\bar{\mathbb{P}}_{F_n}^i \end{Bmatrix} \\ &= 0 \end{aligned} \quad (3.41)$$

The solution for a certain step $n+1$ follows by solving Eq. (3.41) iteratively until reaching convergence, i.e. the vector of residuals $\{d\bar{U}_n \quad d\bar{P}_n \quad d\bar{P}_{F_n}^i\}^T$ at iteration i is smaller than a pre-defined tolerance. The Jacobian term J is a non-symmetric matrix given by

$$\begin{aligned}
 J &= \begin{bmatrix} \frac{\partial \Psi_U}{\partial \bar{U}} & \frac{\partial \Psi_U}{\partial \bar{P}} & \frac{\partial \Psi_U}{\partial \bar{P}_F} \\ \frac{\partial \Psi_P}{\partial \bar{U}} & \frac{\partial \Psi_P}{\partial \bar{P}} & \frac{\partial \Psi_P}{\partial \bar{P}_F} \\ \frac{\partial \Psi_{\bar{P}_F}}{\partial \bar{U}} & \frac{\partial \Psi_{\bar{P}_F}}{\partial \bar{P}} & \frac{\partial \Psi_{\bar{P}_F}}{\partial \bar{P}_F} \end{bmatrix} \\
 &= \begin{bmatrix} \mathbf{K} + \frac{\partial \mathbf{f}_U^{\text{int}}}{\partial \bar{U}} & -\mathbf{Q} + \frac{\partial \mathbf{f}_U^{\text{int}}}{\partial \bar{P}} & \frac{\partial \mathbf{f}_U^{\text{int}}}{\partial \bar{P}_F} \\ \frac{1}{\Delta t} \mathbf{Q}^T & (\mathbf{H} + \mathbf{L1}) & -\mathbf{L2} \\ -\frac{\partial \mathbf{q}_{\bar{P}_F}^{\text{int}}}{\partial \bar{U}} & -\mathbf{L2}^T - \frac{\partial \mathbf{q}_{\bar{P}_F}^{\text{int}}}{\partial \bar{P}} & (\mathbf{H}_F + \mathbf{L3}) - \frac{\partial \mathbf{q}_{\bar{P}_F}^{\text{int}}}{\partial \bar{P}_F} \end{bmatrix} \quad (3.42)
 \end{aligned}$$

In order to optimize computations, the Jacobian may be transformed into a symmetric matrix (Khoëi *et al.*, 2014). Both the definition of the terms and the changes on the matrix are presented in Annex B. As a result, the implemented Jacobian matrix is

$$J = \begin{bmatrix} \mathbf{K} + \mathbf{T} & -\mathbf{Q} & -\mathbf{Q}_F \\ -\mathbf{Q}^T & -\Delta t(\mathbf{H} + \mathbf{L1}) & \Delta t. \mathbf{L2} \\ -\mathbf{Q}_F^T & \Delta t. \mathbf{L2}^T & -\Delta t. (\mathbf{H}_F + \mathbf{L3}) \end{bmatrix} \quad (3.43)$$

Scaling of the Jacobian in Eq. (3.43) is possible for as many enriched degrees of freedom of displacement (β and γ), pore-pressure (δ and ζ) as present in the model (see Annex B for example). Therefore, the integrals that compose the Jacobian are

$$\mathbf{K}_{\beta\gamma} = \int_{\Omega} (\mathbf{B}_u^\beta)^T \mathbf{D} \mathbf{B}_u^\gamma d\Omega \quad (3.44)$$

$$\mathbf{T}_{\beta\gamma} = \int_{\Gamma_d} \llbracket \mathbf{N}_u^\beta \rrbracket^T \mathbf{D}_F \llbracket \mathbf{N}_u^\gamma \rrbracket d\Gamma \quad (3.45)$$

$$\mathbf{Q}_{\beta\zeta} = \int_{\Omega} (\mathbf{B}_u^\beta)^T \mathbf{m} \mathbf{N}_p^\zeta d\Omega \quad (3.46)$$

$$\mathbf{Q}_{F\beta P_F} = \int_{\Omega} \llbracket \mathbf{N}_u^\beta \rrbracket^T \mathbf{n}_{\Gamma d} \mathbf{N}_{P_F}^{\text{std}} d\Omega \quad (3.47)$$

$$\mathbf{H}_{\delta\zeta} = \int_{\Omega} (\mathbf{B}_p^\delta)^T k_F \mathbf{B}_p^\zeta d\Omega \quad (3.48)$$

$$\mathbf{L1}_{\delta\zeta} = \int_{\Gamma_d} (\mathbf{N}_p^\delta)^T c \mathbf{N}_p^\zeta d\Gamma \quad (3.49)$$

$$\mathbf{L2}_{\delta p_F} = \int_{\Gamma_d} (\mathbf{N}_p^\delta)^T c \mathbf{N}_{p_F}^{\text{std}} d\Gamma \quad (3.50)$$

$$\mathbf{L3} = \int_{\Gamma_d} (\mathbf{N}_{p_F}^{\text{std}})^T c \mathbf{N}_{p_F}^{\text{std}} d\Gamma \quad (3.51)$$

$$\mathbf{H}_F = \int_{\Gamma_d} (\mathbf{B}_{p_F}^{\text{std}})^T \mathbf{t}_{\Gamma_d} (2h) k_{Fd} \mathbf{B}_{p_F}^{\text{std}} \mathbf{t}_{\Gamma_d} d\Gamma \quad (3.52)$$

with $\mathbf{m} = \{1 \ 1 \ 0\}^T$. Moreover, the following integrals are used to compute Eqs. (3.38), (3.39) and (3.40).

$$\mathbf{f}_\beta^{\text{ext}} = \int_{\Gamma_t} (\mathbf{N}_u^\beta)^T \bar{t} d\Gamma \quad (3.53)$$

$$\mathbf{q}_\delta^{\text{ext}} = \int_{\Gamma_w} (\mathbf{N}_p^\delta)^T \bar{q}_w d\Gamma \quad (3.54)$$

$$\mathbf{f}_\beta^{\text{int}} = \int_{\Gamma_d} \llbracket \mathbf{N}_u^\beta \rrbracket^T \mathbf{D}_F \bar{\beta} d\Gamma - \int_{\Gamma_d} \llbracket \mathbf{N}_u^\beta \rrbracket^T (p_F \mathbf{n}_{\Gamma_d}) d\Gamma \quad (3.55)$$

$$\mathbf{q}_{p_F}^{\text{int}} = \int_{\Gamma_d} (\mathbf{N}_{p_F}^{\text{std}})^T \mathbf{t}_{\Gamma_d} (2h) \langle \nabla \dot{u} \rangle \mathbf{t}_{\Gamma_d} d\Gamma + \int_{\Gamma_d} (\mathbf{N}_{p_F}^{\text{std}})^T \llbracket \dot{u} \rrbracket \mathbf{n}_{\Gamma_d} d\Gamma \quad (3.56)$$

3.6. Fracture constitutive behaviour

3.6.1. Contact penalty method

When studying interaction between fractures, it is expected that the relative displacements between fracture faces vary considerably. For example, while a hydraulic fracture approaches a natural fracture, compression and friction between the natural fracture faces may occur. However, right after the intersection between hydraulic and natural fracture, the fluid starts filling and pressurizing the natural fracture faces, resulting in a separation of its faces. Therefore, the difference of behaviour that occurs between compression and separation must be correctly modelled.

A formulation based on the contact penalty method limits fracture closure in this work. This method assumes the following conditions, known as the standard Kuhn-Tucker conditions (Khoei, 2008).

$$g_N \geq 0 \quad (3.57)$$

$$t_N \leq 0 \quad (3.58)$$

$$g_N \cdot t_N = 0 \quad (3.59)$$

Eq. (3.57) indicates that the normal fracture opening $g_N = \llbracket u \rrbracket n_{\Gamma_d}$ cannot be negative, i.e. no superposition of faces occurs. Eq. (3.58) governs the normal tractions on the interface, which must always be compressive. Finally, Eq. (3.59) designates that the normal tractions on the interface vanish when there is a gap, i.e. the fracture is open.

The contact constraints are guaranteed through the integral of the fracture material constitutive matrix \mathbf{T} in Eq. (3.45), where the stiffness matrix \mathbf{D}_F is defined by the tangential and normal stiffness, k_t and k_n , respectively.

$$\mathbf{D}_F = \begin{bmatrix} k_t & 0 \\ 0 & k_n \end{bmatrix} \quad (3.60)$$

In the case of a compressive traction on the fracture faces, the value of the normal stiffness k_n takes the value of a penalty factor. The accuracy of satisfying contact constraints highly depends on the penalty factor, which should take an order of magnitude higher than the deformability of the surrounding medium. The larger the value of the penalty parameter, the more accurate contact constraints are. However, very large values for the penalty parameter result in an ill conditioned formulation (Khoei, 2008).

Another evident limitation of this method exists when intersections are modelled. Figure 3.13a shows an eventual fracture intersection and the integration points of each fracture that are closer to the intersection. The colour scheme indicates that each integration point only avoids fracture superposition in its corresponding fracture, i.e. only fracture faces with the same colour check the contact against each other. When a state of deformation similar to the presented in Figure 3.13b is obtained, the contact model is applied between faces of each fracture (yellow faces and green faces do not overlap) but it is not applied in the intersection (yellow and green faces overlap with red and blue faces, respectively). Therefore, a superposition, represented by an orange region in Figure 3.13b, exists in the model.

Although being an important effect in certain cases, in this research it is considered that this limitation does not have a strong influence in hydraulic fracture models, where the fractures tend to open as intersections are created (due to fluid pressure) and contact is less likely to occur.

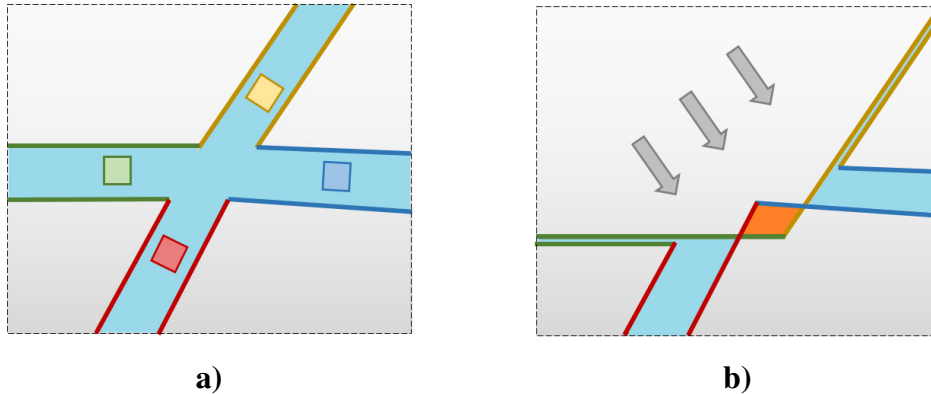


Figure 3.13 – Zoom of an intersection and fractures integration points.
a) Situation with all fractures opened. b) Situation of contact between fractures

3.6.2. Mohr-Coulomb model

Simulation of frictional behaviour of natural fractures adopts a Mohr-Coulomb model for discontinuities. The formulation of this model is based on the research by Rueda *et al.* (2014). The Mohr-Coulomb model is an elastoplastic constitutive model with a failure surface represented by a function f , seen in Figure 3.14 and given by Eq. (3.61).

$$f = \tau + \sigma'_n \times \tan \varphi' - c' \quad (3.61)$$

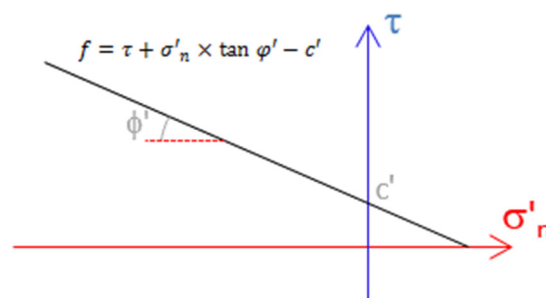


Figure 3.14 – Mohr Coulomb failure surface

where τ is the shear stress, σ'_n the normal stress, φ' the effective friction angle and c' the effective cohesion of the fracture filling.

Additionally, a tensile cut-off failure surface f_n is defined to limit tension stresses, as Eq. (3.62) and Figure 3.15 show.

$$f_n = \sigma'_n - R_t \quad (3.62)$$

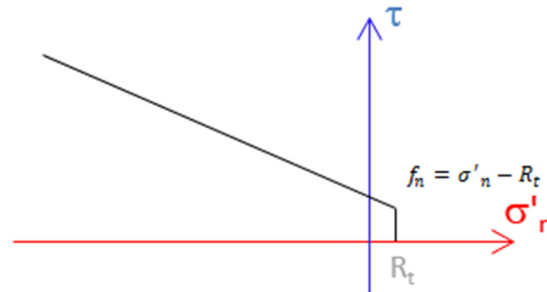


Figure 3.15 – Tensile cut-off failure surface

The constitutive model must define both an elastoplastic stiffness matrix and the stress state, considering the actual deformation state. As the final stress state is not known a-priori, an implicit procedure is used. In this work both functions (3.61) and (3.62) are verified to check if plastic deformations occur. If f or f_n are positive, it means the stress state σ_{trial} is not admissible, so it should be corrected and the plastic deformations computed. Two correction paths are formulated, vertical and perpendicular to the failure surface, as seen in Figure 3.16. The first may be called a non-associated formulation without occurrence of dilatation, while the second is an associated formulation.

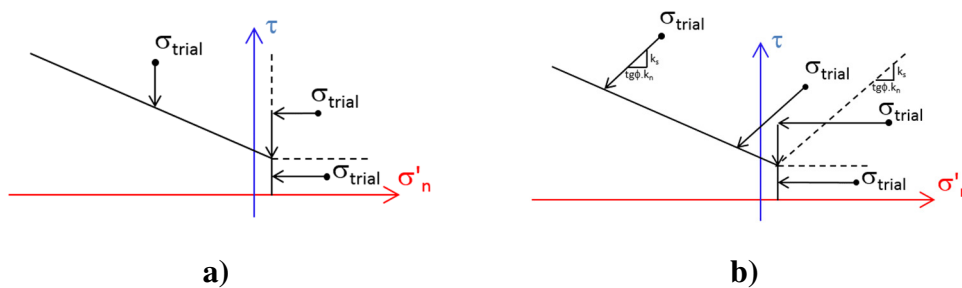


Figure 3.16 – Return paths for Mohr Coulomb model. a) vertical return.

b) perpendicular return

The final change in stress state and the elastoplastic stiffness are given by Eq. (3.63) and Eq. (3.64), respectively.

$$\{\Delta\sigma\} = [D^e]\{\Delta\varepsilon\} - [D^e]\{\Delta\varepsilon^p\} = [D^e]\{\Delta\varepsilon\} - [D^e]\lambda \left\{ \frac{\partial g}{\partial \sigma} \right\} \quad (3.63)$$

$$[D^{ep}] = [D^e] - \frac{[D^e] \left\{ \frac{\partial g}{\partial \sigma} \right\} \left\{ \frac{\partial f}{\partial \sigma} \right\}^T [D^e]}{\left\{ \frac{\partial f}{\partial \sigma} \right\}^T [D^e] \left\{ \frac{\partial g}{\partial \sigma} \right\}} \quad (3.64)$$

where $[D^e]$ is the elastic stiffness matrix, given in Eq. (3.60) and

- $\left\{ \frac{\partial f}{\partial \sigma} \right\}$ is the derivative of the failure surface
 - Mohr Coulomb surface: $\left\{ \frac{\partial f}{\partial \sigma} \right\} = \left\{ \begin{matrix} 1 \\ \tan \varphi' \end{matrix} \right\}$
 - Tensile cut-off surface: $\left\{ \frac{\partial f_n}{\partial \sigma} \right\} = \left\{ \begin{matrix} 0 \\ 1 \end{matrix} \right\}$
- $\left\{ \frac{\partial g}{\partial \sigma} \right\}$ is the derivative of the plastic potential function
 - Mohr Coulomb surface:
 - Vertical return: $\left\{ \frac{\partial g}{\partial \sigma} \right\} = \left\{ \begin{matrix} 1 \\ 0 \end{matrix} \right\}$
 - Perpendicular return: $\left\{ \frac{\partial g}{\partial \sigma} \right\} = \left\{ \begin{matrix} 1 \\ \tan \varphi' \end{matrix} \right\}$
 - Tensile cut-off surface: $\left\{ \frac{\partial g_n}{\partial \sigma} \right\} = \left\{ \begin{matrix} 0 \\ 1 \end{matrix} \right\}$
- Λ is a parameter that guarantees that $f(\sigma_{trial}) = 0$
 - Mohr Coulomb surface:
 - Vertical return: $\Lambda = \frac{f(\sigma^{trial})}{k_s}$
 - Perpendicular return: $\Lambda = \frac{f(\sigma^{trial})}{k_s + k_n \cdot \tan^2 \varphi'}$
 - Tensile cut-off surface: $\Lambda = \frac{f_n(\sigma^{trial})}{k_n}$